

El presente archive corresponde al postprint del artículo publicado en la revista:

Physics and Chemistry of Minerals 38 (7): 543-556 (2011)

Springer-Verlag 2011 DOI 10.1007/s00269-011-0426-3

Recibido: 23 August 2010; Aceptado: 23 March 2011; Publicado online: 9 April 2011

## **Electrical conductivity of polycrystalline Mg(OH)<sub>2</sub> at 2 GPa: effect of grain boundary hydration–dehydration**

Julien Gasc (1), Fabrice Brunet (1, 4) , Nikolai Bagdassarov (2) and Victor Morales-Flórez (3)

(1) Laboratoire de Géologie, Ecole normale supérieure, CNRS-UMR 8538, Paris, France

(2) Institut für Geowissenschaften, Goethe Universität, Frankfurt a. Main, Germany

(3) Instituto de Ciencia de Materiales de Sevilla, Centro de Investigaciones de la Cartuja, Sevilla, Spain

(4) ISTERre, CNRS, Université J. Fourier, BP 53, 38041 Grenoble Cedex 9, France

### **Abstract**

The effect of intergranular water on the conductivity of polycrystalline brucite, Mg(OH)<sub>2</sub>, was investigated using impedance spectroscopy at 2 GPa, during consecutive heating–cooling cycles in the 298–980 K range. The grain boundary hydration levels tested here span water activities from around unity (wet conditions) down to 10<sup>−4</sup> (dry conditions) depending on temperature. Four orders of magnitude in water activity result in electrical conductivity variations for about 6–7 orders of magnitude at 2 GPa and room temperature. Wet brucite samples containing, initially, about 18 wt% of evaporable water (i.e. totally removed at temperatures below 393 K in air), display electrical conductivity values above 10<sup>−2</sup>–10<sup>−3</sup> S/m. A.C. electrical conductivity as a function of temperature follows an Arrhenius behaviour with an activation energy of 0.11 eV. The electrical conductivity of the same polycrystalline brucite material dried beforehand at 393 K (dry conditions) is lower by about 5–6 orders of

magnitude at room temperature and possesses an activation energy of 0.8–0.9 eV which is close to that of protonic diffusion in (001) brucitic planes. Above ca. 873 K, a non-reversible conductivity jump is observed which is interpreted as a water transfer from mineral bulk to grain boundaries (i.e. partial dehydration). Cooling of such partially dehydrated sample shows electrical conductivities much higher than those of the initially dry sample by 4 orders of magnitude at 500 K. Furthermore, the corresponding activation energy is decreased by a factor of about four (i.e. 0.21 eV). Buffering of the sample at low water activity has been achieved by adding CaO or MgO, two hygroscopic compounds, to the starting material. Then, sample conductivities reached the lowest values encountered in this study with the activation energy of 1.1 eV. The strong dependency of the electrical conductivity with water activity highlights the importance of the latter parameter as a controlling factor of diffusion rates in natural processes where water availability and activity may vary grandly. Water exchange between mineral bulk and mineral boundary suggests that grain boundary can be treated as an independent phase in dehydroxylation reactions.

## **Keywords**

Polycrystalline brucite Dehydration reaction Impedance spectroscopy Grain boundary Protonic electrical conductivity Water activity High pressure and temperature

## **Introduction**

The absence or presence of water even at a level of trace amounts at mineral grain boundaries may drastically affect the intergranular diffusion in polymineralic rocks and, consequently, may strongly influence their physical and chemical properties (e.g. Griggs 1967; Rubie 1986; Tullis and Yund 1989). For instance, experiments on the diffusion rate of chemical species show that by adding trace amounts of water to dry polycrystalline enstatite, the diffusivity through the polycrystalline matrix increases by 3–4 orders of magnitude (Milke et al. 2007). Similarly, the rate of grain boundary diffusion of Al in rocks has been shown to vary by seven orders of magnitude depending on water activity (Carlson 2010). The ionic electrical conductivity of polycrystalline materials involves the transport of chemical species at grain boundaries (GB), and therefore, it can be strongly enhanced by the presence of water. For example, in the Earth's crust where most of the rock-forming minerals are insulators, the presence of interconnected grain boundary films containing water strongly affects magneto-telluric and geoelectric data (e.g. Olhoeft 1981; Kurtz et al. 1986; Hyndman and Shearer 1989; Wannamaker et al. 1989). At ambient pressure, the sensitivity of electrical conductivity to water located at grain boundaries has been demonstrated experimentally for a variety of polycrystalline ceramic materials, e.g. LiNiVO<sub>4</sub> and LiCoVO<sub>4</sub> (Kazakopoulos et al. 2008), Li<sub>3</sub>VO<sub>4</sub> (Kazakopoulos and Kalogirou 2009), K<sup>+</sup>-β-ferrite (Ito et al. 1996), CsH<sub>2</sub>PO<sub>4</sub> (Boysen et al. 2003), KHSO<sub>4</sub> (Bagdassarov and Lentz 2005), CsHSO<sub>4</sub> (Bagdassarov 2011). These studies have pointed out that the magnitude of the effect of GB water on grain boundary conductivity depends on water film thickness (Kazakopoulos et al. 2008) and composition (Karus et al. 2000; Ito et al. 1996) as well as on the powder microstructure (Kazakopoulos et al. 2008).

The alternative current (A.C.) electrical conductivity appears to be a powerful tool to investigate the role of variable water concentrations at GB on the transport kinetics of charge carriers, i.e. on their chemical diffusivity, if these charge carriers are ions, protons or molecules. The information about GB transport properties is especially valuable under geologically relevant pressures and temperatures. In particular, the

electrical impedance spectroscopy at high pressures can be used to separate the contribution of grain bulk and grain boundary conductivities in a polycrystalline aggregate that allows to categorize between different dielectric dispersion processes with differing relaxation times (e.g. Hinrichs and daJornada 1997; Zhu et al. 2001; Ter Heege and Renner 2007; He et al. 2007).

This work aims to study the effect of variable amounts of water at grain boundaries and the effect of GB hydration on the transport rate of electrical charge carriers in polycrystalline brucite,  $\text{Mg}(\text{OH})_2$ , by using in situ impedance spectroscopy in a piston-cylinder apparatus, at 2 GPa, and temperatures to 980 K.

Two cases of grain boundary hydration defined in Rubie (1986) have been investigated here: fluid saturated and fluid undersaturated. In the latter case, water in the sample is no longer expressed as a free phase and is only present as GB water in the form of surface molecular  $\text{H}_2\text{O}$  or OH-groups as well as hydroxyl/molecular water in the mineral structure. Contrary to the recent work of Fuji-Ta et al. (2007) on the electrical conductivity of brucite, the present experiments have been conducted in a nominally open system. The absence of a sealed container in the present experiments implies the possibility of water to exchange between sample and pressure assembly. The hydration levels investigated here are therefore only transient, and the corresponding water activity is neither controlled nor constant with time. However, a set of the impedance spectroscopy measurements have been carried out under controlled water activity by adding CaO or MgO to the starting material. This type of strategy is inspired from the work of Urai (1983) who added  $\text{MgCl}_2 \cdot 4\text{H}_2\text{O}$  to polycrystalline bischofite in order to remove adsorbed water.

Polycrystalline brucite,  $\text{Mg}(\text{OH})_2$ , is chosen here because:

olycrystalline brucite,  $\text{Mg}(\text{OH})_2$ , is chosen here because:

1. It is a water-bearing phase that can therefore potentially exchange water with its grain surface;
2. Its dehydration behaviour has already been studied at ambient and high pressures by many authors using a wide variety of techniques (Freund 1967; Gieseke et al. 1970; Yamaoka et al. 1970; Irving et al. 1977; Chen and Fong 1977; Green 1983; Hrabě and Svetík 1985; Kanzaki 1991; Freund 1992; Johnson and Walker 1993; Fukui et al. 2005; Fuji-Ta et al. 2007);
3. A number of rock-forming sheet silicates, for example serpentine minerals, have brucitic layers as a structural unit;
4. The interactions between water and brucite surface have been investigated recently using molecular dynamics (Wang et al. 2004, 2006);
5. Proton conductivity in brucite has been studied at ambient pressure as a function of temperature (Freund 1967; Freund and Wengeler 1980; Wengeler et al. 1980) and under the effect of an applied electric field at the conditions of brucite dehydroxylation (MacKenzie 1973; Kalinichenko and Litovchenko 2000).

### **‘Water’ at grain boundary**

In the range of high lithostatic pressures and temperatures, the original pores in rocks are closed, and water has been expelled (dewatering, Walther and Orville 1982). The remaining porosity of rocks at high P–T conditions is not well-constrained but is expected to be significantly lower than 0.1% (e.g. Norton and Knapp 1977). Some variable amounts of water can still be stored in the intergranular rock space which separates mineral surfaces in polycrystalline aggregates where thin films of water of variable thickness can be formed. For instance, the film thickness reaches 85–185 nm in the case of a (111) NaCl surface in contact with a CaF<sub>2</sub> (111) face under a contact pressure of a few MPa at room temperature (de Meer et al. 2002, 2005). For silicate minerals, the thickness of the intergranular film has been measured to be in the order of a nanometer (Pashley and Kitchener 1979; Heidug 1995; Alcantar et al. 2003). Water in such thin film is structured by electrostatic interaction with the nearby mineral surfaces, and the surface water diffusion is consequently slower than of the bulk liquid water (Mullis 1993; Renard et al. 1999; Alcantar et al. 2003). Vigil et al. (1994) demonstrated that in the case of quartz, a hydrated silica-gel composed of silanol and silicic acid chains can form at the mineral surface.

Brucite that has a layered structure with sheets of Mg-octahedra stacked parallel to (001) with hydrogen bonding between layers crystallizes in the form of platelets with dominant (001) surfaces. The (001) brucite surface is electrostatically neutral and hydrophilic. Because Mg has a +2 charge, every octahedral site in the layer is occupied. This relationship is referred to as ‘trioctahedral’. Because each OH<sup>–</sup> is shared between three octahedra, all the charge is neutralized in a single sheet and so adjacent octahedral sheets are only weakly bonded to one another (Zigan and Rothbauer 1967). Molecular dynamics (MD) simulation shows that the structure of water confined between two (001) brucite surfaces is modified in comparison to bulk water, over distances as large as 15 Å, i.e. about 5 molecular water monolayers (Wang et al. 2004). MD also shows that the water self-diffusion decreases with lowering the absorbed water coverage on (001) brucite surfaces (Wang et al. 2006).

The microscopic description of water structure and diffusivity at GB can be related to the general notion of grain boundary hydration–dehydration used in this study. As it is indicated by Rubie (1986), there is a critical water–rock ratio below which all water excluding the structural water in hydrous minerals is stored at the GB either as an ‘adsorbed’ water, e.g. in a form of double monolayer (for details, see Walther and Orville 1982), or as a water ‘dissolved’ within the GB itself (Vernon 1976). By definition, the molecular arrangement of this GB water differs from that of the bulk liquid water, and so do the transport properties. Above this critical water–rock ratio, free water occurs as an independent phase with bulk liquid water properties. Below this water–rock threshold ratio, the grain boundary can still be hydrated, although the rock is fluid-unsaturated (for details see the definition of hydrous but fluid-unsaturated conditions in Carlson 2010). Carlson (2010) introduces the notion of the intergranular water activity. Ultimately, in hypothetical dry rocks that would contain no water at all, the grain boundary could be totally anhydrous. Fully anhydrous GB conditions cannot be achieved, here, especially during Mg(OH)<sub>2</sub> dehydration since brucite is a hydrous mineral that can potentially act as a water reservoir for the GB. The minimum GB water activity that can be reached is that buffered by the MgO—Mg(OH)<sub>2</sub> equilibrium in the absence of free water, i.e. below the Mg(OH)<sub>2</sub> dehydration temperature.

The present work deals with a series of Mg(OH)<sub>2</sub> partial dehydration experiments at high pressure in the open system with variable water activity and the in situ measurements of the electrical conductivity.

## Starting materials and methods

### Starting material and hydration level

The starting material consisted of fine-grained brucite powder (1–10  $\mu\text{m}$ ) synthesized under hydrothermal conditions from MgO oxide (fired MgCO<sub>3</sub>, reagent grade, at 1,273 K for 2 h) and ~50 wt% of H<sub>2</sub>O at 623 K and 150 MPa in a cold-seal vessel (gold container). The moisture of the sample used for impedance spectroscopy measurements was measured by thermogravimetric analyses (TGA) in a STD Q600 experimental device. The sample (10–20 mg) was placed in a platinum crucible, and the experiments were carried out under a nitrogen flux of 100.0 ml/min, starting from ambient temperature up to 1,073 K with a heating rate of 10°C/min.

Three levels of starting material moisture were achieved (Table 1):

1.

The brucite powder was kept in contact with air after the hydrothermal synthesis without applying any specific drying treatment. TGA data (Fig. 1) shows that about 18 wt% of H<sub>2</sub>O is removed from the sample below 373 K ('evaporable water'). Part of this 'evaporable water' is expected to 'feed' the sample GB upon compression up to 2 GPa. A second dehydration step starts above 573 K which is consistent with the loss of structural water associated with the decomposition of brucite into periclase (MgO) + water (Fig. 1). Upon compression up to 2 GPa and due to porosity reduction, part of the intergranular and absorbed water will remain between brucite grains, i.e. at the grain boundary. This type of sample will be named with the prefix Wet followed by the run number.

2.

When the synthesized brucite powder is dried at 373 K, all the 'evaporable water' is removed from the sample. This is illustrated by TGA measurements on a sample dried at 373 K overnight (Fig. 1). Weight loss associated with water removal is observed only above 573 K, when the structural water is released due to brucite dehydration. The prefix Dry will be used to refer to this type of sample here below.

3.

Similar hydration level as (2) was investigated by adding either CaO obtained by firing CaCO<sub>3</sub> (Reagent Grade®) at 1,273 K (CaO-Chem samples) or MgO from Mg-hydrocarbonate (Reagent Grade®) fired at 1,273 K for 12 h (MgO-Chem samples). The hygroscopic character of CaO is used to achieve a very low and constant water activity (around 10<sup>-4</sup>) in the course of the in situ impedance spectroscopy measurements. Similarly, MgO is added to the sample in order to buffer at high P–T conditions the water activity with the Mg(OH)<sub>2</sub>—MgO pair (see "Appendix"). The characteristics of the starting materials are summarized in Table 1.

## Impedance spectroscopy set-up

The electrical conductivity measurements have been carried out in a piston cylinder apparatus at 2 GPa (a detailed description of the set-up is found in Bagdassarov et al. 2001). Electrical impedance measurements  $<100 \text{ M}\Omega$  have been performed with the use of a Solartron® 1260 Phase-Gain-Analyzer interfaced with a PC. In high-pressure experiments, a 1-Volt sine signal is applied in the 0.1 Hz to 200 kHz frequency range. For measurements of impedance  $>100 \text{ M}\Omega$ , Broad Band Dielectric Converter Novocontrol® with variable RC-reference set has been used.

A cell for electrical impedance measurements represents a coaxial cylindrical capacitor (with a geometric factor varied between 5.8 and 7.0 cm) filled with a pressed powder sample (Fig. 2). The diameter of the inner electrode is 2.2 mm, and the diameter of the outer electrode is 4.1 mm. The temperature is measured using a S-type thermocouple without pressure correction. The electrodes are made of a Pt-foil (0.05 mm thickness). During impedance measurements, the piston-cylinder press is separated from the ground of the Solartron 1260 device. One of the thermoelements and the mass of the high-pressure autoclave are used to connect the measuring device and the cell electrodes. Prior to the high-pressure experiments, a measuring cell has been calibrated against the impedances of a short and an open circuit in the 500 kHz–0.01 Hz frequency range. A typical AC-resistance of the cell to a short circuit is  $0.4 \text{ }\Omega$ . These calibrations have been taken into account to calculate electrical capacitance and impedance as a function of frequency. Temperature control was operated manually in order to avoid electrical noise coming from the firing angle controller.

## Conductivity data processing and interpretation

Each measured frequency scan of the complex resistance  $Z^*(\omega)$  has been fitted to the following expression (e.g. Jonscher 1991):

$$Z^* = R_1 + (j \cdot \omega \cdot \tau_1)^{\alpha_{\text{HF}}} + R_2 + (j \cdot \omega \cdot \tau_2)^{\alpha_{\text{LFD}}},$$

where the first and the second terms are responsible for high and low frequency dielectric losses, i.e. to two arcs on an Argand-type diagram describing bulk, and grain boundary + electrode polarization processes. In Eq. 1, parameters  $0 < \alpha_{\text{HF}}, \alpha_{\text{LFD}} < 1$  are empirical constants characterizing the deviation of the observed dielectric loss peaks from a Debye-type function. Parameters  $\tau_1, R_1$  and  $\alpha_{\text{HF}}$  are related to the bulk properties of sample or material properties measured at a high frequency range (HF). The  $\alpha_{\text{HF}}$  parameter describes the power law dispersion in a situation where the short-range displacements of lattice defects become coupled with ionic environment. In ionic conductors with increasing temperature,  $\alpha_{\text{HF}}$  may decrease from 1 down to 0.3–0.5. The second term in Eq. 1 is called low frequency dispersion (LFD, see Jonscher 1991). The parameters  $R_2, \tau_2$  and  $\alpha_{\text{LFD}}$  depend on grain boundary conductivity and on electrode polarization process and, thus, traditionally have been omitted from the electrical impedance analysis. Frequency scans of the electrical impedance of brucite samples obtained

during heating and cooling cycles were plotted in an Argand-type diagram, i.e. the dependence of  $-\text{Im}[Z^*]$  versus  $\text{Re}[Z^*]$ . The fitting procedure to Eq. 1 has been done using Novocontrol® software.

When water is present at grain boundary, the contribution from the second term in Eq. 1 (low frequency dispersion) may vary drastically. The amplitude of the second arc depends on size, shape and connectivity of GB and their conductivity relative to the grain interiors (Macdonald 1987). At low volume fraction of conductive GB (volume fraction of GB  $\sim 1$  vol.%, relative GB conductivity 103 higher than grain interior), only one arc can be resolved in Argand plots (McLachan et al. 2000). When GB are dry and their volume  $\sim 10\%$ , the low frequency arc in Argand plots corresponding to the second term in Eq. 1 becomes very large, and the grain interior term cannot be resolved from impedance spectra. Two arcs with the same amplitude correspond to the case when the volume fraction of GB is small and they are more resistive than the grain interior (McLachan et al. 2000; Campo et al. 2002). The presence of two types of GB, more conductive (for example, with water) and less conductive (e.g. dry), results in a complicated Argand plots where the low frequency arc is extended in the case when the majority of GB are less conductive and dry or in a perfect low frequency semicircle in the case when the majority of grain boundaries are conductive and wet (Feig and Maier 1999). The overall conductivity will be enhanced due to continuous GB possessing low impedance. The presence of a continuous and conductive GB phase leads to the introduction of a second time constant in the equivalent circuit in Eq. 1 which will be larger than bulk dielectric relaxation time and smaller than the time constant of electrode polarization. In the case of dry and poorly conductive GB, the contribution of the low dispersion term in Eq. 1 to the overall conductivity will be negligible, and the GB arc may be effectively hidden by electrode polarization arc. Depending on the geometry of the conductive GB phase, whether it is lenticular or continuous, the position of GB arc may approach low or high frequency on Argand plot (Macdonald 1987). During dehydration of mineral grains, not only the relative conductivity of GB may vary with time, but also the dielectric constant  $\epsilon$ . Water saturation of GB results in higher  $\epsilon$  (at 20°C,  $\epsilon$  of water is 81,  $\epsilon$  for MgO  $\sim 9.8$  and  $\epsilon$  for Mg(OH)<sub>2</sub>  $\sim 7.7$ , from Rosenholtz and Smith 1936) and shifts the GB arc to lower frequency.

### Characterization of the recovered samples

Part of the recovered sample after impedance spectroscopy measurements at HP-HT was grinded under ethanol in an agate mortar for X-ray powder diffraction, whereas the rest was embedded in epoxy, cut and polished (using ethanol instead of water) for further scanning electron microscope (SEM) characterization. X-ray diffraction patterns were collected using a rotating anode (Rigaku diffractometer at ENS) with an acceleration voltage set to 50 kV and 300 mA, using acquisition time of 1°/min. The BRASS 2.0 software (Burzlaff and Hountas 1982) was used to evaluate phase proportions using the Rietveld method. SEM imaging and qualitative analysis by energy-dispersive spectrometry (EDS) were achieved using a Zeiss Sigma™ field-emission-gun SEM (FE-SEM) equipped with a large-area (50 mm<sup>2</sup>) EDS silicon drift detector, X-Max Oxford Instruments, at ENS (Paris).

## Results

### HP-HT impedance spectroscopy measurement

All conductivity data are plotted on Fig. 3 using an Arrhenius type diagram ( $\ln [\sigma T]$  vs.  $1/T$ ). Measurements were started at room temperature (RT) after cold compression of the sample up to 2 GPa, even though the quality of these first data might be hampered by improper sintering of the sample powder. Wet and Dry brucite samples show highly contrasted conductivities (Table 1) at RT (2 GPa),  $\sigma = 10^{-2}$ – $10^{-3}$  S/m for Wet1 and Wet2 and  $\sigma = 10^{-9}$  S/m for Dry1, CaO-Chem1 and CaO-Chem2. The presence of excess water apparently controls the conductivity of the brucite samples at RT more than the addition of CaO which seems to have very little effect on the starting sample conductivity under these conditions. After the cold compression stage, samples were heated stepwise (heating rate of 2.5–3 K/min in average), and the impedance data were collected every 50 K. The  $\ln [\sigma T]$  parameter for Wet1 (and Wet2) is found to increase linearly as a function of the reciprocal temperature (Fig. 3) from ambient to about 803 K (the corresponding activation energy is 0.11 eV). Above 803 K, the dependency of the Wet1 electrical conductivity with temperature is significantly different (higher apparent activation energy is found above 803 K). The conductivity of Wet1 is not reversed upon cooling (cooling ramp of 3.5–4 K/min in average) after 13.6 h at 843 K. The activation energy has increased to 0.39 eV (Fig. 3; Table 1) what led to a final conductivity of  $10^{-6}$  S/m at room temperature after the heating/cooling cycle (i.e. closer to the initial RT conductivity of the dried samples). In the case of the Wet2 experiment for which impedance data were collected upon cooling readily after the first heating cycle, reversibility was achieved. Again, when after a second heating ramp, the sample (Wet2) was kept at constant temperature (937 K) for 12 h, the second cooling cycle led to much lower conductivity values (non-reversibility).

The Dry1 sample has been subjected to two heating/cooling cycles (Fig. 3; Table 1), a first one below 781 K and a second one where the sample reached a maximum temperature of 932 K. Along the first heating ramp, conductivity depends on reciprocal temperature according to the Arrhenian equation with an activation energy of 0.87 eV, and it is perfectly reversible upon cooling. The conductivity behaviour of the Dry1 sample is confirmed by a second heating cycle up to 932 K. The sample was maintained at this temperature at 925 K for 12 h; higher conductivity values were then encountered, below ca. 773 K, along the second cooling ramp, and much lower activation energy (ca. 0.21 eV) was then retrieved.

Both CaO-Chem1 and CaO-Chem2 samples show the same conductivity behaviour despite a different CaO content. A positive conductivity jump is observed upon heating at about 443–453 K. On the contrary, from 623 to 823 K, a conductivity decrease is observed during slow heating or annealing of the sample (Fig. 3). The  $\sigma T$  values for CaO-Chem1 (and CaO-Chem2) upon cooling from 803 to 813 K down to room temperature (at 2 GPa) display an Arrhenian behaviour with a relatively high activation energy of 1.1 eV (Fig. 3). Before being cooled, CaO-Chem2 was heated up to 953 K. This resulted in a huge  $\sigma T$  increase with an apparent activation of energy to 3.9 eV. Then, upon cooling, the conductivity of CaO-Chem2 was found to be identical to that of CaO-Chem1 although the latter sample did not experience the 823–953 K stage.

Conductivity values obtained for MgO-Chem3 for the first heating cycle up to 790 K are close to those found for Dry1 (Fig. 3). Upon cooling of the sample after ageing for 12 h at 790 K, the MgO-Chem3 conductivity approaches that of CaO-Chem1 (and CaO-Chem2) and appears to be reversible when an additional heating/cooling cycle is applied. Similar activation energy of 1.14 eV was found for  $\sigma T$  of this sample (Fig. 3; Table 1).



## Sample characterization after HP-HT conductivity measurement

Samples characterization was carried out on the quenched samples after HP-HT impedance spectroscopy measurements. The recovered sample is made of brucite grains that form platelets displaying prismatic sections on polished mounts (Fig. 4) of around  $1 \times 3 \mu\text{m}^2$  (Table 1) with thin longitudinal cleavages. Brucite platelets are expected to align preferentially perpendicular to the piston stroke direction during the first stages of compression (slight preferred orientation is observed on SEM images, Fig. 4c). Consequently, according to the electrode set-up (Fig. 2), conduction parallel to the (001) brucite crystallographic planes will tend to be favoured. No significant porosity could be detected using FE-SEM (i.e. low porosity, below the per cent level), and no wetted grain boundaries are observed, even for wet samples (see Fig. 4). A homogeneous dispersion of the CaO component, added to the starting material, is observed in CaO-Chem1 (Fig. 4b), and the Ca-rich clusters are not connected. They form spherical aggregates of a few  $\mu\text{m}$ . Within these aggregates, minerals with fibrous textures are interpreted as the hydration products of CaO to portlandite. These spherical aggregates are surrounded by smaller calcium bearing grains with sizes of about 500 nm which are likely to be the result of the (late?) carbonation of either CaO and/or portlandite grains (Fig. 4c).

## X-ray powder diffraction

The refinement of CaO-Chem1 pattern confirms the presence of brucite,  $\text{Mg}(\text{OH})_2$ , as the main constituent phase along with portlandite,  $\text{Ca}(\text{OH})_2$  and periclase, MgO, which are present, within uncertainty, in the same molar amount (around 7 mol %). The same holds true for CaO-Chem2 where  $\text{Ca}(\text{OH})_2$  and MgO represent ca. 2 and 3 mol %, respectively.

For the Wet1 sample (CaO- and MgO-free starting material), only a tiny MgO reflexion is observed (Fig. 5), the intensity of which is about 150 counts. Rietveld refinement is not suitable for estimating such small amount of MgO (below 1 mol %). For comparison, when CaO is added (CaO-Chem1 and CaO-Chem2), this MgO reflexion has a much higher intensity (i.e. by approximately 80 times, normalized to the 001 brucite reflexion). The quench MgO-Chem3 sample (Fig. 5) is composed of ca. 7.5 mol % (5–6 wt%) of MgO. This value is significantly lower than the nominal amount of MgO initially added to the sample (10 wt%) due to partial hydration during the run or later in the course of sample preparation for XRD. Dry1 and Wet2 diffraction patterns show no evidence for the presence of MgO. Although brucite partial dehydration probably occurred in these experiments, subsequent rehydration affected these samples.

## Discussion

### Effect of brucite dehydration on electrical conductivity

Fuji-Ta et al. (2007) have measured the D.C. electrical conductivity (at a single frequency of 10 mHz) of  $\text{Mg}(\text{OH})_2$  powder that has been dried beforehand at 500 K over  $\frac{1}{2}$  h. The powder sample was enclosed in a single-crystal sapphire container leading to undrained conditions, whereas, here, water can escape from the experimental charge (drained or slowly drained conditions, see below). Their results confirm the measurements of Gieseke et al. (1970) at low frequencies. However, it must be noted that the activation energy of electrical conductivity derived from a single

frequency measurement may contain a large error. The conductivity values obtained here (Fig. 3) during the first heating/cooling cycle (i.e. below 773 K) are consistent with those retrieved by Fuji-Ta et al. (2007) in the course of their first heating cycle. The second heating cycle up to 932 K led to identical conductivity values and confirmed an Arrhenian behaviour up to ca. 873 K. Above that temperature, the  $\sigma T$  parameter seems to increase with a steeper slope in the Arrhenius plot (Fig. 3). Such a change in the apparent activation energy has been documented by Fuji-Ta et al. (2007), and it was interpreted as the effect of brucite partial dehydration. Both the results of Fuji-Ta et al. (2007) and the present data show that the conductivity of the partially dehydrated sample remains high in comparison with dry brucite even when temperature is decreased below the brucite ‘dehydration point’ (Fig. 3). Therefore, measurements performed under open and close conditions seem to converge. Even when a sample was held for 12 h at 925 K, the dehydration fluid was still partly kept at the grain boundaries, and high conductivity values were still measured. These high conductivity values are comparable with those documented by Fuji-Ta et al. (2007) under undrained conditions. This indicates slow drain rates that are comparable with the timescale of impedance spectroscopy measurements. Overall, these two high-pressure conductivity datasets collected under undrained and partially drained conditions indicate that the water released upon the sample dehydration does not entirely return to the crystal structure. The released water is partially deposited in GB, and thereby, it influences the overall impedance properties of the sample. The activation energy values estimated by Fuji-Ta et al. (2007), 0.3 eV, and retrieved here, 0.21 eV (partially dehydrated Dry1 sample), are higher than the protonic conductivity in de-ionized water 0.10–0.17 eV (Zheng et al. 1997; Moore et al. 2008). This may exclude the effect of free water on the sample-electrode interface.

#### Conductivity under water saturated conditions

Wet1 and Wet2 samples that contained initially more than 15 wt% ‘evaporable water’ can be used as a reference for the role of water as a conductive medium in a polycrystalline brucite aggregate at 2 GPa and various temperatures. Furthermore, these runs can be used to investigate the residence time of free water, OH-groups and H<sup>+</sup> in the sample. The conductivities of Wet1 and Wet2 samples are mutually consistent and are characterized by a relatively high conductivity at RT and 2 GPa,  $\sigma = 10^{-2}$ – $10^{-3}$  S/m, associated with a relatively low activation energy of 0.11 eV which compares very well with the activation energy of protonic conductivity in de-ionized water (e.g. 0.10–0.17 eV; Zheng et al. 1997). The full reversibility of the conductivity data is verified with the use of Wet2 sample. In this sample, a first heating and cooling cycle was continuously run at temperatures from 300 to 775 K and back to 300 K. After the second heating cycle, the sample was annealed for 12 h at 937 K. During a consecutive cooling of Wet2 sample (Fig. 3), the measured conductivity values and corresponding activation energy are close to those which were measured in Dry1 sample and not very different from those reported by Fuji-Ta et al. (2007) in their first heating cycle. Ageing of Wet2 sample at 2 GPa and 937 K for 12 h produces basically the same effect on conductivity as a drying of the sample beforehand at 393 K (see Dry1 sample) or drying at 500 K at ambient pressure (Fuji-Ta et al. 2007). Figure 6 represents the impedance spectra of the studied samples at different temperatures during heating and cooling cycles. This figure depicts the evolution of Bode- or Argand-diagram  $-\text{Im}[Z_s]$  versus  $\text{Re}[Z_s]$  in Wet1 sample. During the first heating, the left semi-cycle (upper left panel Fig. 6) is significantly depressed, a HF  $\approx$  0.3–0.4, which may be interpreted as a very wide distribution of RC-parameters in equivalent circuit. This left arc represents low resistance of grain bulk and grain boundaries of Wet1 sample. After annealing of Wet1 sample at 843 K during 13.6 h, the spectra changed (right panel, Fig 6); the bulk resistance becomes larger and a HF equals around 0.85–0.9. This indicates an approximately unique dielectric relaxation process with a rather narrow

statistics of RC-elements in equivalent circuit, i.e. bulk of grains. At the same time, there is a small plateau between left bulk arc and the right electrode polarization arc which may be interpreted as a small unresolved GB arc. This arc indicates small GB resistance and an increase of the dielectric relaxation time of grain boundary RC-elements. It can be concluded that the bulk interior becomes significantly less conductive, GB boundaries become more conductive and the dielectric constant  $\epsilon$  of GB is much larger than in the grain interior. Here, one can speculate that grain boundaries are still conductive and contain some water or hydrogen, but they are not well interconnected or their volume fraction is small.

### Conductivity at low water activity

Experiments CaO-Chem1, CaO-Chem2 and MgO-Chem3 were designed to test the sample conductivity at low and buffered water activities. All these three samples have been submitted to the same drying treatment in an oven as for Dry1 sample. It is therefore not surprising that their initial conductivity at room temperature and 2 GPa (1.5 and 1.4 G $\Omega$  for CaO-Chem1 and CaO-Chem2, respectively) is closer to that of Dry1 rather than to that of Wet1 and Wet2. The presence of CaO or MgO imposes a low water activity in the sample (Appendix). However, it has obvious shortcomings with respect to the characterization of the brucite conductivity; (1) the addition of an extra compound can modify the conductivity of the sample and (2) CaO reacts with H<sub>2</sub>O and Mg(OH)<sub>2</sub> to form Ca(OH)<sub>2</sub> and MgO (Appendix) what induces conductivity changes during the heating cycle. The non-Arrhenian behaviour of the conductivity of both CaO-Chem1 and CaO-Chem2 during heating (Fig. 3) is interpreted as resulting from these chemical reactions and will not be discussed here. In order to achieve these reactions to be completed and to avoid reactive transient effects during the conductivity measurements, CaO-Chem1 and CaO-Chem2 have been submitted to constant pressure and temperature conditions for several hours; 14 h at 813 K and 12 h at 828 K, respectively. Similar transient effects, although less pronounced, were observed in the MgO-Chem3 run having a slope kink in the Arrhenius plot between 573 and 673 K. At these temperatures, during the first heating cycle, the conductivity data for MgO-Chem3 started to deviate (towards smaller values) from those of Dry1 (Fig. 3). Therefore, it is likely that temperatures above 573 K are required for buffering the water activity using the MgO/Mg(OH)<sub>2</sub> pair.

After ageing at high temperature, CaO-Chem1 and CaO-Chem2 were cooled down to the RT (Table 1). Conductivity measurements show a well-defined and reversible Arrhenius dependency with a kink at 803 K. Below this temperature, the same conductivity values were obtained in the two experiments with samples having different amounts of added CaO (Fig. 3). The corresponding value of the activation energy is 1.1 eV (Table 1). Similarly, after ageing the MgO-Chem3 sample at 790 K for 12 h, sample conductivity showed a well-defined and reversible Arrhenian behaviour (1.14 eV). The second heating/cooling cycle up to 924 K confirms this behaviour and shows that the kink at 803 K, observed in the Arrhenius plot for CaO-Chem1 and CaO-Chem2, is absent. Therefore, this conductivity feature around 803 K is specific for samples containing CaO (and portlandite) and could be merely due to Ca(OH)<sub>2</sub> decomposition/melting (e.g. Lin et al. 2009).

### Implications for transport at Mg(OH)<sub>2</sub> grain boundary

The effect of two initial hydration levels (wet and dry) on the impedance properties of polycrystalline brucite has been investigated at 2 GPa following heating and cooling cycles in the 298–980 K range (Fig. 3; Table 1) under drained conditions but with relatively slow drain rates (see above). The hydration levels investigated here span water activities from unity (saturated GB, Wet1 and Wet2 samples) down to  $10^{-4}$  depending on temperature (dry GB, Chem1, 2 and 3). SEM characterization of the samples after experiments at 2 GPa does not allow to notice any measurable porosity owing to sharp grain boundary contacts. Four orders of magnitude in water activity correspond to the conductivity differences for  $\sim 6$  orders of magnitude at 2 GPa and room temperature (Table 1). Due to higher activation energy for conduction mechanisms associated to dry conditions (0.9–1.1 eV), the conductivity contrast between wet and dry conditions decreases with increasing temperature and cancels out when approaching 1,173 K. The Wet1 and Wet2 experiments are characterized by a high conductivity ( $10^{-2}$ – $10^{-3}$  S/m) and a low activation energy (0.11 eV or 12 kJ/mol) which is close to the activation energy of protonic conductivity in de-ionized water (e.g. 0.10–0.17 eV; Zheng et al. 1997).

The predominance of GB conductivity may be proved by comparing the frequency corresponding to the cusp in the sample impedance spectra (Figs. 6, 7). Data collected upon heating of Wet1, when plotted on an Argand plot (Fig. 6), clearly show that the bulk component of the electrical resistance is even smaller than the low frequency dispersion (right semi-cycle on the Argand plots).

The lowest conductivity values and the highest activation energies (around 1–1.1 eV) are encountered for the thermally and chemically dried samples (Dry and Chem, respectively) for which the amount of GB water is expected to be minimum. When displayed on an Argand plot (Fig. 7), impedance data collected in the course of CaO-Chem1 during heating–cooling cycles indicate that the grain boundary resistance is very small; the plateau between right and left semi-cycles is negligible. The parameter  $\alpha$  HF that characterizes the dispersion of dielectric relaxation processes becomes close to 0.9–0.95 upon cooling. This is an indication that the bulk dielectric relaxation is almost of a Debye type (or a single relaxation mechanism) and that the contribution from GB conductivity is effectively depressed when GB are chemically dried.

When brucite samples are dried thermally beforehand (e.g. Dry1 or Fuji-Ta et al. 2007), they display larger conductivity values with smaller activation energy (around 0.9 eV). The same activation energy has been found for the diffusion rate of slow protons in brucite (MacKenzie 1973; Wengeler et al. 1980). This suggests that, in the dry samples, the charge carriers are mostly tunnelling protons (Freund 1992) which migrate through the brucite grains and perpendicular to the stacking direction of the octahedral layers. Lowering of the sample conductivity in experiments containing Ca(OH)<sub>2</sub> or MgO might arise from (1) the blocking effect of this additional material or (2) a decrease in the GB transport rate between two grains due to severe drying.

The conductivity jump observed above 803 K in this study and by Fuji-Ta et al. (2007) strongly suggests that water is transferred from bulk to grain boundary beyond a given temperature. If the driving force for such water transfer is thermochemical, this would support the notion of chemical equilibrium between grain interior and grain boundary (Hiraga et al. 2004), the latter being considered then as an independent phase.

The conductivity difference between the partially dehydrated sample (Dry1—second cooling, Fig. 3) and the Wet samples and the difference in activation energy (0.2 and 0.11 eV, respectively) may arise from an increase in the GB thickness related to a higher amount of intergranular

water. Alternatively, in the case of the partially dehydrated sample, the differences of GB conductivity may result from the overall stronger mineral surface—water interactions. The hydrophilic (001) cleavage surface of brucite is protonated, and additional water molecules (interfacial water) can be physisorbed onto it (e.g. Sakuma et al. 2003 and references therein). Wang et al. (2004) modelled (MD simulation) the structure of water confined in nanopores between (001) brucite surfaces. They found that profiles of oxygen and hydrogen atomic density as well as H<sub>2</sub>O dipole orientation show significant deviation from the corresponding structural properties of bulk water to distances as large as 15 Å (i.e. 5 molecular water layers) from the surface. Furthermore, it has been shown that transport rates are lowered in structured water (Churakov et al. 2004); the partially dehydrated sample would then have structured water in its intergranular space, whereas the Wet samples would rather have mostly free water. Finally, one can also argue that the brucite dehydration kinetics that supplies water into the intergranular space leads to the formation of differing solid products, i.e. Mg(OH)<sub>2-x</sub>O<sub>x/2</sub> (Freund and Sperling 1976) with differing amount of impurities and structural defects (Green 1983), which in turn can influence the sample conductivity.

### **Concluding remarks**

1.

Although the experimental set-up used in this study is chemically opened with respect to the water component, the electrical conductivity measurements clearly show that significant amounts of water can be retained in sample GB for many hours at temperatures up to 980 K, i.e. for a timescale that exceeds that of the impedance spectroscopy measurements. The present experimental set-up allowed to reproduce HP–HT conductivity data in the course of partial dehydration. These results complement the measurements in a closed system on encapsulated brucite (Fuji-Ta et al. 2007).

2.

The present work demonstrated a significant role of GB water which cannot be ignored when measuring the electrical conductivity of hydrous minerals. The present experiments confirm the fact that the rate-determining factor for the overall dehydroxylation reaction is the HOH transport through GB, rather than through crystal lattice (Chen and Fong 1977).

3.

Hydrous phases, in drained and undrained measurement set-ups, may exchange water with their grain boundaries at temperatures far below the dehydration temperature defined for saturated conditions.

4.

The use of solid water-activity buffer in combination with the electrical impedance spectroscopy has proved that it is a possible way (1) to control the GB hydration and (2) to derive the bulk contribution to the electrical conductivity of polycrystalline hydrous materials.

5.

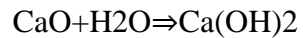
Finally, the effect of water on the transport kinetics at grain boundary outlined here is in line with recent work on Al diffusivity in metamorphic rocks as a function of water activity. Carlson (2010) showed that rates of Al intergranular diffusion may vary, at constant temperature, by as much as seven orders of magnitude in the range of H<sub>2</sub>O activities encountered in metamorphic processes.

### **Acknowledgments**

This work was partly supported by the SYSTER funding program (INSU-CNRS). Travel expenses were covered by the PROCOPE (0938RJ) French–German exchange program. Reviews by J. Renner and C.J. Peach helped substantially improve the manuscript. N. Findling is warmly thanked for his help at running FE-SEM and XRD at ENS. We also acknowledge the technical service of the Instituto de Ciencia de Materiales de Sevilla (CSIC-US).

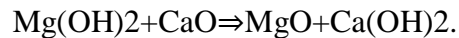
### **Appendix**

The hydration of CaO will remove free water from the sample according to the following reaction:



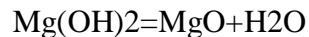
(A1)

After that reaction has occurred, remaining CaO will also dehydrate brucite as follows



(A2)

The two compounds MgO and Mg(OH)<sub>2</sub> will coexist (as in MgO-Chem3) in the sample and buffer the water activity according to the following equilibrium:



(A3)

Under equilibrium conditions, the Gibbs free energy of Reaction A3 is

$$\Delta G_{T,P} = \Delta G^0(T,P) + RT \cdot \ln(a_{\text{H}_2\text{O}}) = 0,$$

(A3)

where  $\Delta G^0(T,P)$  is the standard state Gibbs free energy of Reaction A3 at T and P.

For instance, at 803 K and 2 GPa, the co-existence of MgO and Mg(OH)<sub>2</sub> buffers the water activity ( $a_{\text{H}_2\text{O}}$ ) to 10<sup>-1</sup>. The buffered water activity—temperature relationship at 2 GPa is displayed in Fig. 8.

## References

1. Alcantar N, Israelachvili J, Boles J (2003) Forces and ionic transport between mica surfaces: Implications for pressure solution. *Geochim Cosmochim Acta* 67(7):1289–1304
2. Bagdassarov N (2011) Phase transitions in CsHSO<sub>4</sub> up to 2.5 GPa: Impedance spectroscopy under pressure. *J Phys Chem Sol* 72:236–244. doi:10.1016/j.jpcs.2011.01.008
3. Bagdassarov N, Lentz G (2005) High pressure behavior of KHSO<sub>4</sub> studied by electrical impedance spectroscopy. *Solid State Commun* 136:16–21
4. Bagdassarov N, Freiheit HC, Putnis A (2001) Ionic conductivity and pressure dependence of trigonal-to-cubic phase transition in lithium sodium sulphate. *Solid State Ionics* 143(3–4):285–296CrossRef
5. Berman RG (1991) Thermobarometry using multi-equilibrium calculations - a new technique, with petrological applications. *Can Mineral* 29:833–855
6. Berman RG, Aranovich LY (1996) Optimized standard state and solution properties of minerals.1. Model calibration for olivine, orthopyroxene, cordierite, garnet, ilmenite in the system FeO-MgO-CaO-Al<sub>2</sub>O<sub>3</sub>-TiO<sub>2</sub>-SiO<sub>2</sub>. *Contrib Mineral Petrol* 126(1–2):1–24
7. Boysen DA, Haile SM, Liu HJ, Secco RA (2003) High-temperature behavior of CsH<sub>2</sub>PO<sub>4</sub> under both ambient and high pressure conditions. *Chem Mater* 15(3):727–736
8. Burzlaff H, Hountas A (1982) Computer program for the derivation of symmetry operations from the space group symbols. *J Appl Crystallogr* 15:464–467
9. Campo MA, Woo LY, Mason TO, Garboczi EJ (2002) Frequency-dependent electrical mixing law behavior in spherical particle composites. *J Electroceram* 9:49–56
10. Carlson WD (2010) Dependence of reaction kinetics on H<sub>2</sub>O activity as inferred from rates of intergranular diffusion of aluminium. *J Metam Geology* 28(7):735–752
11. Chen DTY, Fong PH (1977) Thermal analysis of magnesium hydroxide. *J Therm Anal* 12:5–13
12. Churakov SV, Ianuzzi M, Parinello M (2004) Ab initio study of dehydroxylation-carbonation reaction on brucite surface. *J Phys Chem B* 108:11567–11574



13. de Meer S, Spiers CJ, Peach CJ, Watanabe T (2002) Diffusive properties of fluid-filled grain boundaries measured electrically during active pressure solution. *Earth Planet Sci Lett* 200(1–2):147–157
14. de Meer S, Spiers CJ, Nakashima S (2005) Structure and diffusive properties of fluid filled grain boundaries: An in situ study using infrared (micro) spectroscopy. *Earth Planet Sci Lett* 232(3–4):403–414
15. Feig J, Maier J (1999) The impedance of ceramics with highly resistive grain boundaries: Validity and limits of brick model. *J Eur Ceram Soc* 19:693–696
16. Freund F (1967) Retention of hydroxyl groups on magnesium oxide. *J Am Ceram Soc* 50(9):493–494
17. Freund F (1992) Highly ionic hydroxides: unexpected proton conductivity in  $\text{Mg}(\text{OH})_2$  and homologues. In: Colombari Ph (ed) *Proton conductors*. Cambridge University Press, Cambridge, pp 138–157
18. Freund F, Sperling V (1976) A magnesium oxide defect structure of hexagonal symmetry. *Mater Res Bull* 11(6):621–629
19. Freund F, Wengeler H (1980) Proton Conductivity of Simple Ionic Hydroxides Part I: The Proton Conductivities of  $\text{Al}(\text{OH})_3$ ,  $\text{Ca}(\text{OH})_2$ , and  $\text{Mg}(\text{OH})_2$ . *Ber Bunsen Phys Chem* 84(9):866–873
20. Fuji-Ta K, Katsura T, Matsuzaki T, Ichiki M (2007) Electrical conductivity measurements of brucite under crustal pressure and temperature conditions. *Earth Planets Space* 59(6):645–648
21. Fukui H, Inoue T, Yasui T, Katsura T, Funakoshi K, Ohtaka O (2005) Decomposition of brucite up to 20 GPa: evidence for high MgO-solubility in the liquid phase. *Eur J Mineral* 17(2):261–267
22. Gieseke W, Nägerl H, Freund F (1970) N-type and defect proton conductivity by  $\text{H}_2\text{O}$  formation in  $\text{Mg}(\text{OH})_2$  lattice. *Naturwissenschaften* 57(10):493
23. Green J (1983) Calcination of precipitated  $\text{Mg}(\text{OH})_2$  to active MgO in the production of refractory and chemical grade MgO. *J Mater Sci* 18(3):637–651
24. Griggs DT (1967) Hydrolytic weakening of quartz and other silicates. *Geophys J* 14:19–31
25. He CY, Gao CX, Ma YZ, Li M, Hao AM, Huang XW, Liu BG, Zhang DM, Yu C, Zou GT, Li YC, Li H, Li XD, Liu J (2007) In situ electrical impedance spectroscopy under high pressure on diamond anvil cell. *Appl Phys Lett*. doi:10.1063/1.2778760
26. Heidug WK (1995) Intergranular solid-fluid phase-transformations under stress—the effect of surface forces. *J Geophys Res-Solid Earth* 100(B4):5931–5940

27. Hinrichs R, daJornada JAH (1997) Piston-cylinder apparatus for high pressure impedance spectroscopy. *Rev Sci Instrum* 68(1):193–196
28. Hiraga T, Anderson IM, Kohlstedt DL (2004) Grain boundaries as reservoirs of incompatible elements in the Earth's mantle. *Nature* 427:699–703
29. Hrabě Z, Svetík Š (1985) The influence of water vapour on decomposition of magnesite and brucite. *Thermochim Acta* 92:653–656
30. Hyndman RD, Shearer PM (1989) Water in the lower continental-crust—modelling magneto telluric and seismic-reflection results. *Geophys J Int* 98(2):343–365
31. Irving AJ, Huang WL, Wyllie PJ (1977) Phase relations of portlandite,  $\text{Ca}(\text{OH})_2$  and brucite,  $\text{Mg}(\text{OH})_2$  to 33 Kilobars. *Am J Sci* 277(3):313–321
32. Ito S, Kurosawa H, Akashi K, Michiue Y, Watanabe M (1996) Crystal structure and electric conductivity of  $\text{K}^+$ -beta-ferrite with ideal composition  $\text{KFe}_{10}\text{O}_{17}$ . *Solid State Ionics* 86–8:745–750
33. Johnson MC, Walker D (1993) Brucite  $[\text{Mg}(\text{OH})_2]$  dehydration and the molar volume of  $\text{H}_2\text{O}$  to 15 GPa. *Am Mineral* 78(3–4):271–284
34. Jonscher AK (1991) Low-frequency dispersion in volume and interfacial situations. *J Mater Sci* 26:1618–1626
35. Kalinichenko EA, Litovchenko AS (2000) Effect of an electric field on brucite dehydroxylation. *Phys Solid State* 42(11):2070–2075
36. Kanzaki M (1991) Dehydration of brucite ( $\text{Mg}(\text{OH})_2$ ) at high-pressures detected by differential thermal-analysis. *Geophys Res Lett* 18(12):2189–2192
37. Karus M, Kalogirou O, Gunsser W, Reller A (2000) The effect of humidity on the conductivity processes in polycrystalline  $\text{Cu}^{2+}$ -stabilised  $\text{K}^+$ -beta  $\text{Fe}^{3+}$ -ferrite. *Solid State Ionics* 136:375–380
38. Kazakopoulos A, Kalogirou O (2009) Effect of humidity on the conduction processes of  $\text{Li}_3\text{VO}_4$ . *J Mater Sci* 44(18):4987–4992
39. Kazakopoulos A, Sarafidis C, Chrissafis K, Kalogirou O (2008) Synthesis and characterization of inverse spinel  $\text{LiNiVO}_4$  and  $\text{LiCoVO}_4$  with impedance spectroscopy. *Solid State Ionics* 179(35–36):1980–1985
40. Kurtz RD, Delaurier JM, Gupta JC (1986) A magneto telluric sounding across Vancouver island detects the subducting Juan-De-Fuca plate. *Nature* 321(6070):596–599
41. Lin S, Wang Y, Suzuki Y (2009) High-Temperature  $\text{CaO}$  hydration/ $\text{Ca}(\text{OH})_2$  decomposition over a multitude of cycles. *Energy & Fuels* 23:2855–2861

42. Macdonald JR (1987) Impedance spectroscopy: emphasizing solid materials and systems. Wiley-Interscience, New York, p 346
43. MacKenzie KJD (1973) Thermal reactions of inorganic hydroxyl-compounds under applied electric fields III: effect of external D.C. fields on proton tunnelling and mass transport. *J Thermal Anal* 5:363–377
44. McLachan DS, Hwang J-H, Mason TO (2000) Evaluating dielectric impedance spectra using effective media theories. *J Electroceram* 5(1):37–51
45. Milke R, Dohmen R, Becker HW, Wirth R (2007) Growth kinetics of enstatite reaction rims studied on nano-scale, Part I: Methodology, microscopic observations and the role of water. *Contrib Mineral Petrol* 154(5):519–533
46. Moore RD, Richards G, Story A (2008) Electrical conductivity as an indicator of water chemistry and hydrologic process. *Streamline Watershed Manag Bull* 11(2):25–29
47. Mullis AM (1993) Determination of the rate-limiting mechanism for quartz pressure dissolution. *Geochim Cosmochim Acta* 57(7):1499–1503
48. Norton D, Knapp R (1977) Transport phenomena in hydrothermal systems; the nature of porosity. *Am J Science* 277:913–936. doi:10.2475/ajs.277.8.913
49. Olhoeft GR (1981) Electrical-properties of granite with implications for the lower crust. *J Geophys Res* 86(NB2):931–936
50. Pashley RM, Kitchener JA (1979) Surface forces in adsorbed multilayers of water on quartz. *J Colloid Interface Sci* 71(3):491–500
51. Renard F, Park A, Ortoleva P, Gratier JP (1999) An integrated model for transitional pressure solution in sandstones. *Tectonophys* 312(2–4):97–115
52. Rosenholtz JL, Smith DT (1936) The dielectric constant of mineral powders. *Am Mineral* 21:115–120
53. Rubie DC (1986) The catalysis of mineral reactions by water and restrictions on the presence of aqueous fluid during metamorphism. *Min Mag* 50(3):399–415
54. Sakuma H, Tsuchiya T, Kawamura K, Otsuki K (2003) Large self-diffusion of water on brucite surface by ab initio potential energy surface and molecular dynamics simulations. *Surf Sci* 536(1–3):L396–L402
55. Ter Heege JH, Renner J (2007) In situ impedance spectroscopy on pyrophyllite and CaCO<sub>3</sub> at high pressure and temperature: phase transformations and kinetics of atomistic transport. *Phys Chem Miner* 34(7):445–465

56. Tullis J, Yund RA (1989) Hydrolytic weakening of quartz aggregates - the effects of water and pressure on recovery. *Geophys Res Lett* 16(11):1343–1346
57. Urai JL (1983) Water assisted dynamic recrystallization and weakening in polycrystalline bischofite. *Tectonophys* 96(1–2):125–157
58. Vernon RH (1976) *Metamorphic processes*. Murby, London, p 247
59. Vigil G, Xu ZH, Steinberg S, Israelachvili J (1994) Interactions of silica surfaces. *J Colloid Interface Sci* 165(2):367–385
60. Walther JV, Orville PM (1982) Volatile production and transport in regional metamorphism. *Contrib Mineral Petrol* 79(3):252–257
61. Wang JW, Kalinichev AG, Kirkpatrick RJ (2004) Molecular modeling of water structure in nano-pores between brucite (001) surfaces. *Geochim Cosmochim Acta* 68(16):3351–3365
62. Wang JW, Kalinichev AG, Kirkpatrick RJ (2006) Effects of substrate structure and composition on the structure, dynamics, and energetics of water at mineral surfaces: A molecular dynamics modeling study. *Geochim Cosmochim Acta* 70(3):562–582
63. Wannamaker PE, Booker JR, Filloux JH et al (1989) Magnetotelluric observations across the Defuca Juan subduction system in the EMSLAB project. *J Geophys Res* 94(B10):14111–14125
64. Wengeler H, Martens R, Freund F (1980) Proton conductivity of simple ionic hydroxides. 2. In situ formation of water-molecules prior to dehydration. *Ber Bunsen Phys Chem* 84(9):873–880
65. Yamaoka S, Fukunaga O, Saito S (1970) Phase equilibrium in system MgO-H<sub>2</sub>O at high temperatures and very high pressures. *J Am Ceram Soc* 53(4):179–182
66. Zheng HF, Xie HS, Xu YS, Song MS, Guo J, Zhang YM (1997) The electrical conductivity of H<sub>2</sub>O at 0.21–4.18 GPa and 20–350 degrees C. *Chin Sci Bull* 42(12):969–976
67. Zhu MX, Xie HS, Guo J, Bai WM, Xu ZM (2001) Impedance spectroscopy analysis on electrical properties of serpentine at high pressure and high temperature. *Sci China Ser D-Earth Sci* 44(4):336–345
68. Zigan F, Rothbauer R (1967) Neutronenbeugungsmessungen am Brucit. *Neues JB Miner* 4:137–143

## Figure captions

**Figure 1.** Results of the thermogravimetric analysis. Sample weight loss (wt%) plotted as a function of the heating ramp temperature (10 K/min)

**Figure 2.** Scheme of the cell for measuring electrical conductivity in a piston-cylinder apparatus (modified after Bagdassarov et al. 2001): 1 inner, 2 outer Pt-foil electrodes, 3 sample, 4 thermocouple capillary, 5 Al<sub>2</sub>O<sub>3</sub> ceramics, 6 graphite heater, 7 CaF<sub>2</sub> sleeve, 8 BN insulating sleeve, 9 AlSiMg ceramics, 10 hard metal core, 11 hard metal piston, 12 stainless steel plug, 13 pyrophyllite, 14 copper contact ring, 15 ground contact

**Figure 3.** Arrhenius plot for all of the electrical conductivity data. Plain symbols correspond to conductivity data collected along the heating cycle, whereas empty symbols represent cooling data. When two temperature cycles were performed, the same symbols are used but of a grey colour to picture the second cycle data. Draw lines represent the linear fit (Arrhenius law) to the data, the slope of which is indicated by the value (eV) in a frame box. a Wet1, Wet2 and Dry1 compared to the 1 GPa data at 10 mHz from Fuji-Ta et al. (2007) on polycrystalline Mg(OH)<sub>2</sub> under undrained conditions (+connected with solid line correspond to the first heating; +connected with dashed line correspond to the heating 2-cycle, and +connected with dashed line correspond to the 5-th heating cycle). Circles, diamonds and triangles correspond to the Wet1, Wet2 and Dry1 experiments, respectively. b Comparison between the electrical conductivities of all the dried samples, either at 393 K in an oven only (Dry1) or both in an oven (393 K) and then chemically under pressure and temperature due to the presence of CaO (CaO-Chem1 and CaO-Chem2) or MgO (MgO-Chem3). Triangles, circles, squares and diamonds stand for the Dry1, CaO-Chem1, CaO-Chem2 and MgO-Chem3 data, respectively

**Figure 4.** FE-SEM images of the recovered samples a Wet1, backscattered electron (BSE) image. Grain size is comprised between 1 and 10 μm. Porosity is apparently very low (less than a few %) and is difficult to estimate due to GB opening upon decompression (and grain removal in the course of polishing). b Overview of CaO-Chem1 (BSE image). Bright areas correspond to Ca-rich phases (mainly Ca hydroxide). Note the development of cracks during decompression. c Details of CaO-Chem1. Ca(OH)<sub>2</sub> is rimmed with small CaCO<sub>3</sub> grains. Slight brucite grain preferred orientation is visible on this image

**Figure 5.** X-ray powder diffraction pattern of Wet1, CaO-Chem1 and CaO-Chem2 and MgO-Chem3 (CuK α radiation). The curve represents the refinement of these patterns using BRASS with three phases (brucite, periclase and portlandite, corresponding symbols are indicated on the figure). Longer accumulation times (by a factor of three) have been used for the Wet1 sample to detect minute amount of MgO

**Figure 6.** Results of the impedance spectroscopy in sample Wet1 (upper panels) and Cao-chem1 (lower panels) during heating (left side panels) and cooling (right side panels). The numbers corresponding to open symbols indicate log frequency values in Hz. Parameters of impedance spectra fitting to Eq. 1: in Wet1 upon heating at 567 K, R<sub>1</sub> = 1.42 × 10<sup>3</sup> Ω, τ<sub>1</sub> = 4.34 × 10<sup>-8</sup> s, α<sub>HF</sub> = 0.36; at 669 K, R<sub>1</sub> = 1.09 × 10<sup>3</sup> Ω, τ<sub>1</sub> = 2.52 × 10<sup>-8</sup> s, α<sub>HF</sub> = 0.45; at 782 K, R<sub>1</sub> = 92 Ω, τ<sub>1</sub> = 1.57 × 10<sup>-8</sup> s, α<sub>HF</sub> = 0.38; upon cooling at 579 K, R<sub>1</sub> = 4.26 × 10<sup>4</sup> Ω, τ<sub>1</sub> = 1.41 × 10<sup>-6</sup>

s,  $\alpha_{HF} = 0.86$ ; at 675 K,  $R_1 = 1.6 \times 10^4 \Omega$ ,  $\tau_1 = 4.33 \times 10^{-7} \text{ s}$ ,  $\alpha_{HF} = 0.84$ ; at 789 K,  $R_1 = 8.64 \times 10^3 \Omega$ ,  $\tau_1 = 2.12 \times 10^{-7} \text{ s}$ ,  $\alpha_{HF} = 0.91$ ; in CaO-Chem1 upon heating at 473 K,  $R_1 = 3.6 \times 10^5 \Omega$ ,  $\tau_1 = 1.52 \times 10^{-5} \text{ s}$ ,  $\alpha_{HF} = 0.66$ ; at 728 K,  $R_1 = 7.61 \times 10^3 \Omega$ ,  $\tau_1 = 2.67 \times 10^{-6} \text{ s}$ ,  $\alpha_{HF} = 0.90$ ; at 823 K,  $R_1 = 1.47 \times 10^3 \Omega$ ,  $\tau_1 = 3.67 \times 10^{-7} \text{ s}$ ,  $\alpha_{HF} = 0.86$ ; upon cooling at 577 K,  $R_1 = 4.39 \times 10^7 \Omega$ ,  $\tau_1 = 1.76 \times 10^{-3} \text{ s}$ ,  $\alpha_{HF} = 0.88$ ; at 673 K,  $R_1 = 1.55 \times 10^6 \Omega$ ,  $\tau_1 = 5.3 \times 10^{-5} \text{ s}$ ,  $\alpha_{HF} = 0.93$ ; at 808 K (not shown),  $R_1 = 3.71 \times 10^4 \Omega$ ,  $\tau_1 = 1.07 \times 10^{-6} \text{ s}$ ,  $\alpha_{HF} = 0.94$ . (subscript s by impedance Z stands for the connection in sequence of constant phase elements in equivalent circuits by fitting the data)

**Figure 7.** Argand diagrams of CaO-Chem2 (upper panels) and MgO-Chem3 (lower panels) during heating (left side panels) and cooling (right side panels). The numbers next to open symbols indicate log frequency values in Hz. In the former case, grain boundaries contribute very little to the overall resistance; the grain boundary phase is presumably discontinuous. In the latter case, the large arc is composed of two poorly resolved arcs. The low frequency arc is overlapped by high frequency arc suggesting that the grain boundary phase possesses a thickness comparable with the grain size due to better sintering after the thermal cycle. Parameters of impedance spectra fitting to Eq. 1: CaO-Chem2 upon heating at 573 K,  $R_1 = 32 \times 10^3 \Omega$ ,  $\tau_1 = 0.9 \times 10^{-6} \text{ s}$ ,  $\alpha_{HF} = 0.84$ ; at 678 K,  $R_1 = 15.4 \times 10^3 \Omega$ ,  $\tau_1 = 4 \times 10^{-7} \text{ s}$ ,  $\alpha_{HF} = 0.89$ ; upon cooling at 676 K,  $R_1 = 2.5 \times 10^6 \Omega$ ,  $\tau_1 = 7.7 \times 10^{-5} \text{ s}$ ,  $\alpha_{HF} = 0.91$ ; at 775 K,  $R_1 = 1.7 \times 10^5 \Omega$ ,  $\tau_1 = 4.8 \times 10^{-6} \text{ s}$ ,  $\alpha_{HF} = 0.97$ ; at 622 K  $R_1 = 12 \times 10^6 \Omega$ ,  $\tau_1 = 4.5 \times 10^{-4} \text{ s}$ ,  $\alpha_{HF} = 0.83$ . In MgO-Chem3 upon heating at 527 K,  $R_1 = 1.45 \times 10^6 \Omega$ ,  $\tau_1 = 4.9 \times 10^{-4} \text{ s}$ ,  $\alpha_{HF} = 0.88$ ; at 575 K,  $R_1 = 4.5 \times 10^6 \Omega$ ,  $\tau_1 = 1.4 \times 10^{-4} \text{ s}$ ,  $\alpha_{HF} = 0.87$ ; at 631 K,  $R_1 = 1.6 \times 10^6 \Omega$ ,  $\tau_1 = 4.9 \times 10^{-5} \text{ s}$ ,  $\alpha_{HF} = 0.9$ ; at 673 K  $R_1 = 0.83 \times 10^6 \Omega$ ,  $\tau_1 = 2.4 \times 10^{-5} \text{ s}$ ,  $\alpha_{HF} = 0.89$ ; upon cooling at 721 K,  $R_1 = 2 \times 10^6 \Omega$ ,  $\tau_1 = 5 \times 10^{-5} \text{ s}$ ,  $\alpha_{HF} = 0.96$ ; at 664 K,  $R_1 = 9.7 \times 10^6 \Omega$ ,  $\tau_1 = 2.5 \times 10^{-4} \text{ s}$ ,  $\alpha_{HF} = 0.96$ ; at 630 K,  $R_1 = 30 \times 10^6 \Omega$ ,  $\tau_1 = 7.8 \times 10^{-4} \text{ s}$ ,  $\alpha_{HF} = 0.95$ . Subscript s in the impedance parameter,  $Z_s$ , stands for the connection in sequence of constant phase elements in equivalent circuits by fitting the data

**Figure 8.** Water activity buffered by the MgO–Mg(OH)<sub>2</sub> assemblage as a function of temperature at 2 GPa calculated using the Wintwq.2.34 software (Berman 1991; Berman and Aranovich 1996)

**Table 1**

Table 1

Starting materials, temperature cycles and impedance spectroscopy results

Run	Starting material	Start. Evap. H <sub>2</sub> O (wt%)	ln ( $\sigma \times T$ ) at RT	Cycle	T <sub>max</sub> (K)	Plateau		E <sub>a</sub> , eV	
						T. K	t. min	Heat	Cool
Wet1	Mg(OH) <sub>2</sub>	18	0.02	1	980	843	815	0.11	0.39
Wet2	Mg(OH) <sub>2</sub>	18	0.08	1	775	–	–	0.11	0.11
				2	937	937	720	0.11	0.47
Dry1	Mg(OH) <sub>2</sub>	Dry	<-13.3	1	781	–	–	0.87	0.87
				2	932	925	720	0.87	0.21
CaO-Chem1	Mg(OH) <sub>2</sub> + CaO (10 wt%)	Dry	-12.9	1	873	813	817	–	1.1
CaO-Chem2	Mg(OH) <sub>2</sub> + CaO (5 wt%)	Dry	-12.6	1	953	828	722	–	1.1
MgO-Chem3	Mg(OH) <sub>2</sub> + MgO (10 wt%)	Dry	-17.0	1	790	790	720	–	1.14
				2	924	913	900	–	1.14

Start. Evap. Starting evaporable water (lost below 373 K), RT room temperature, Heat heating cycle, Cool cooling cycle

Figure 1

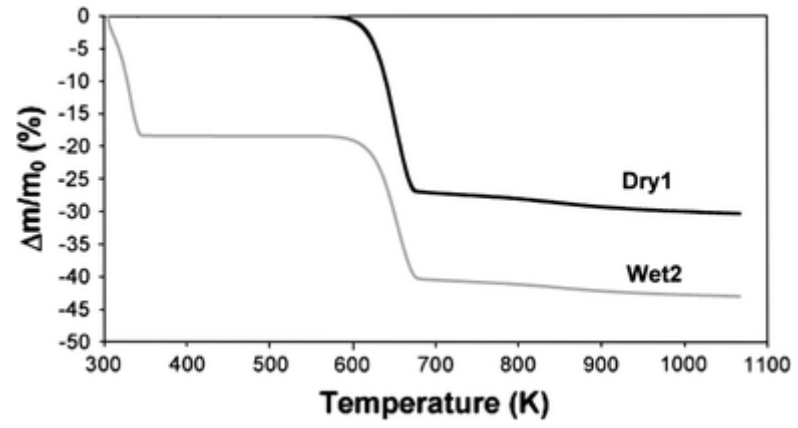
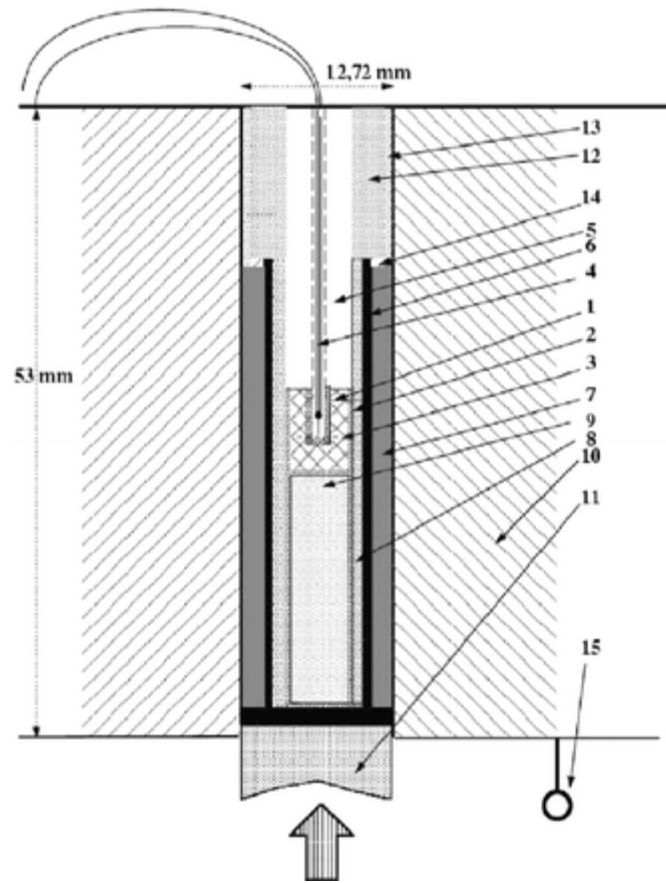




Figure 2



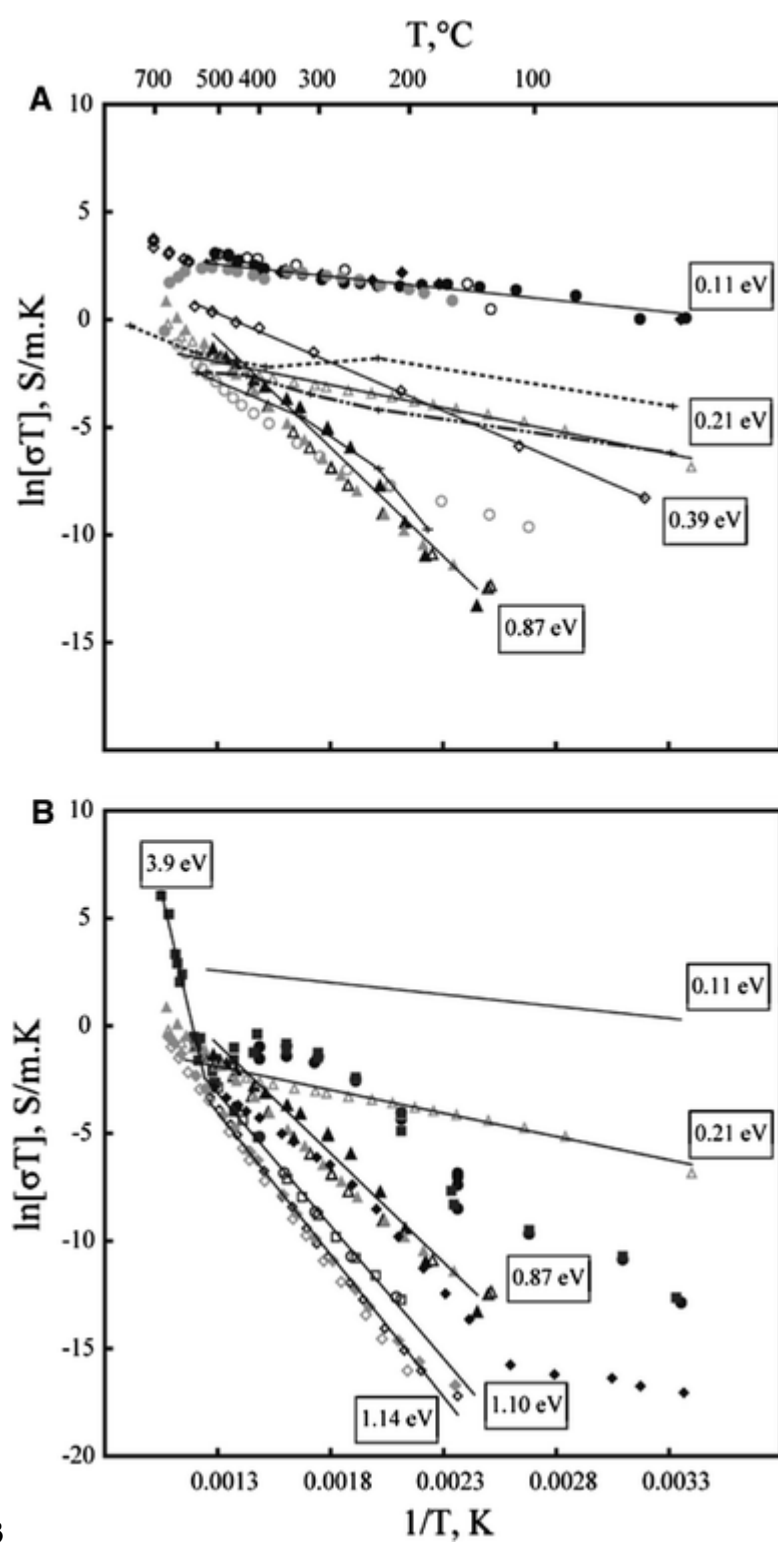
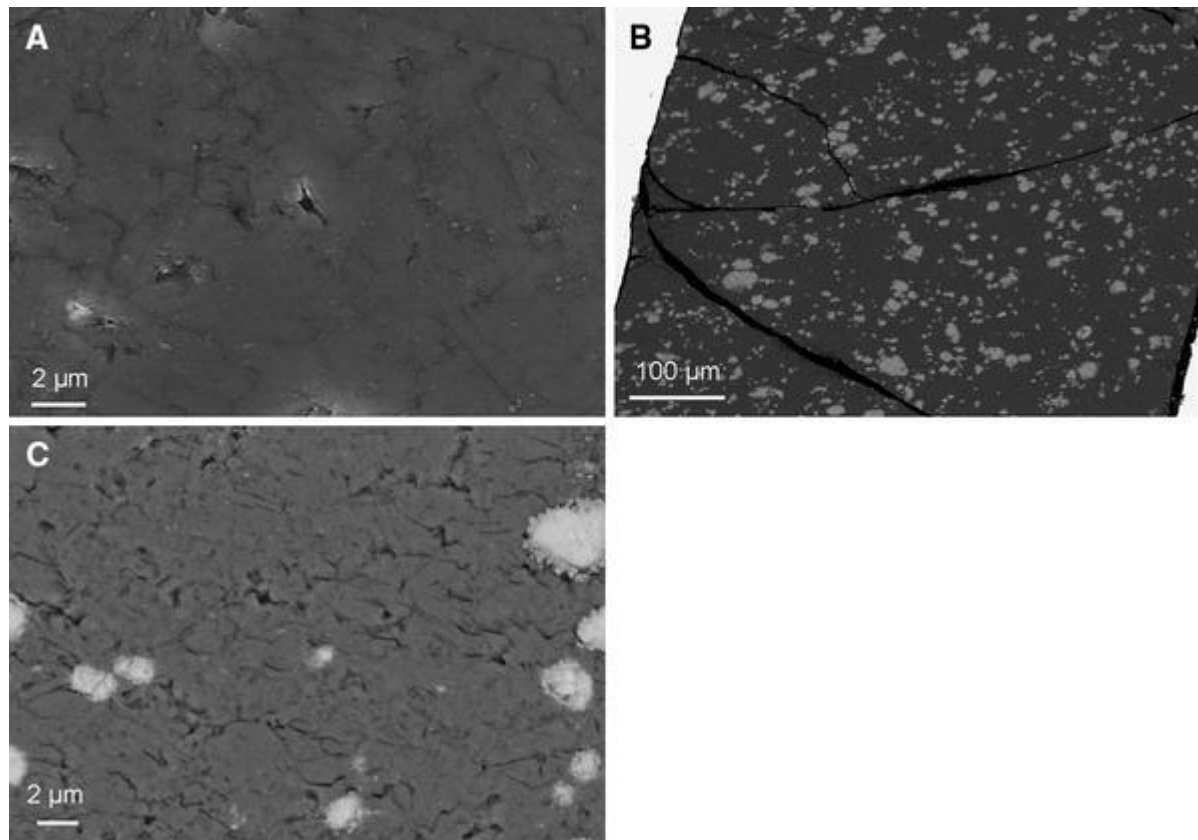


Figure 3

**Figure 4**



**Fig. 4**

Figure 5

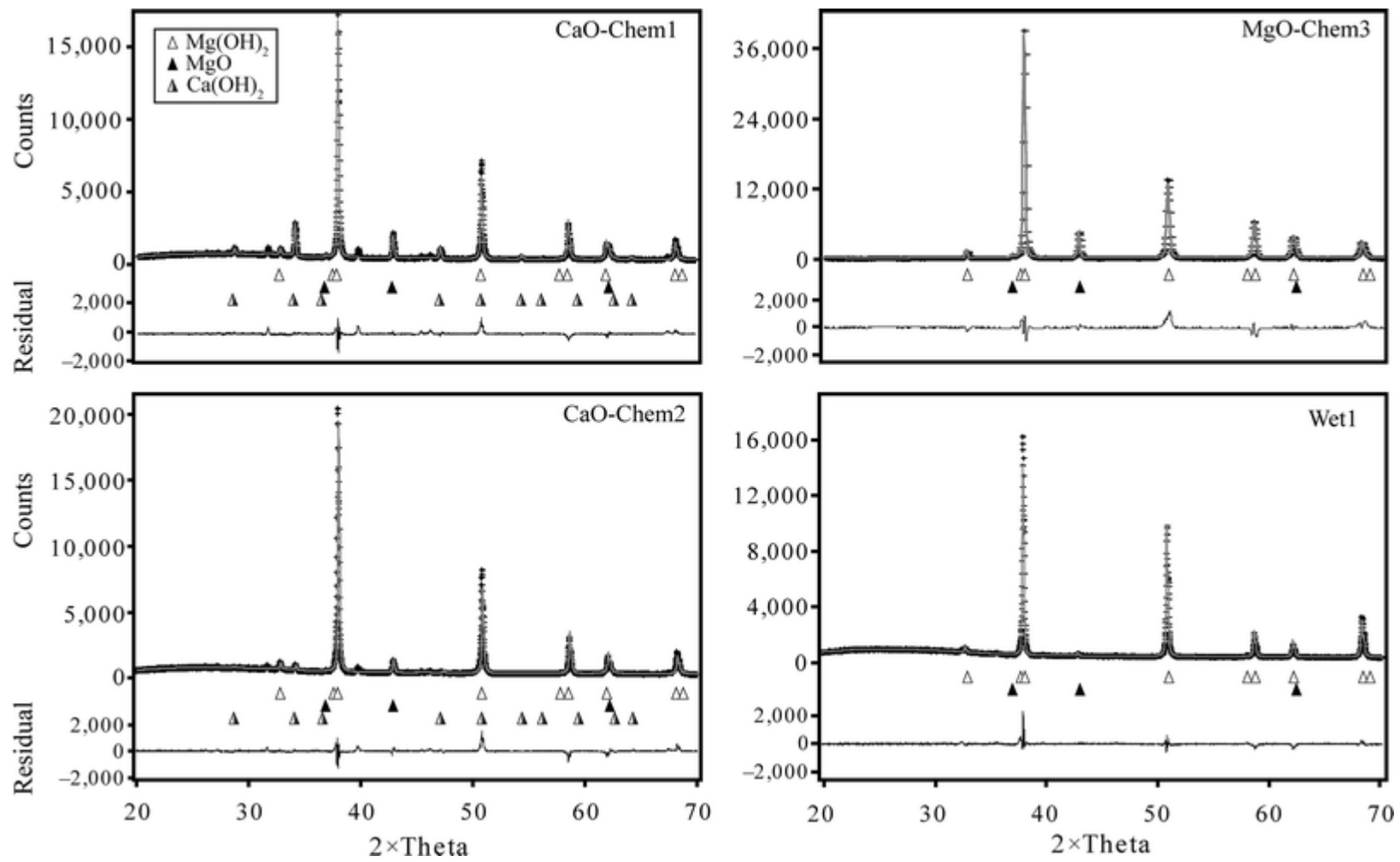


Figure 6

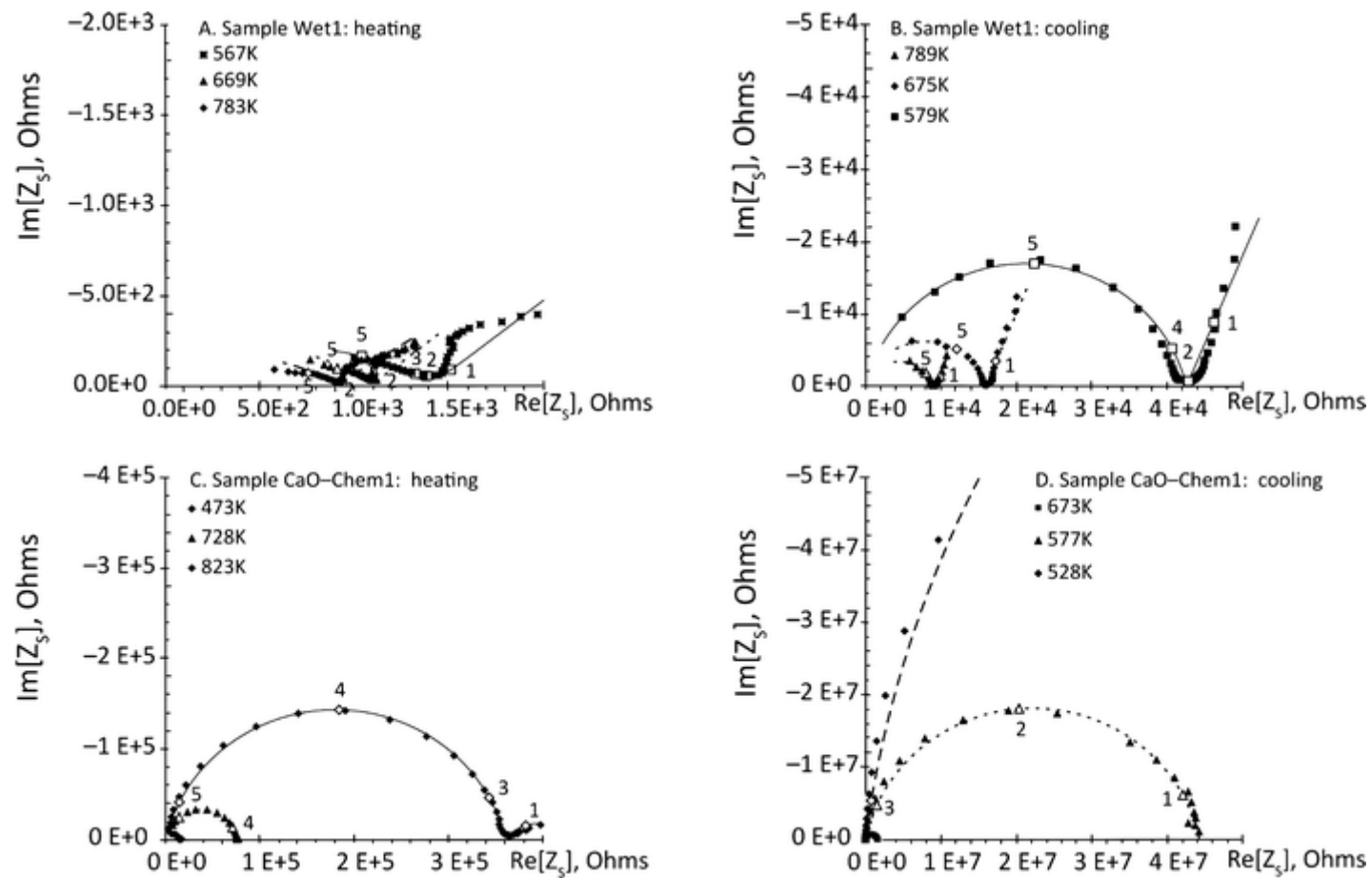


Figure 7

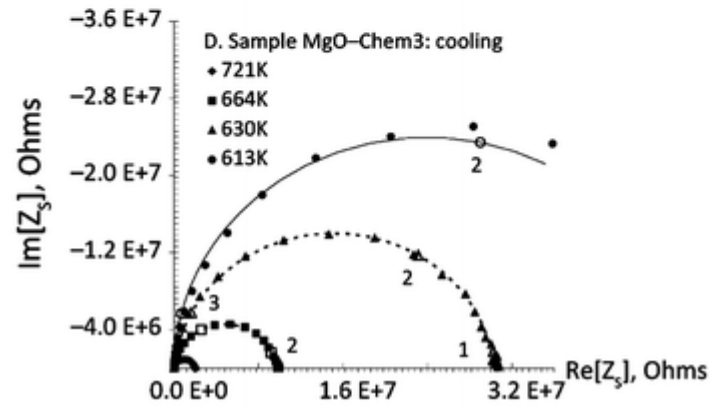
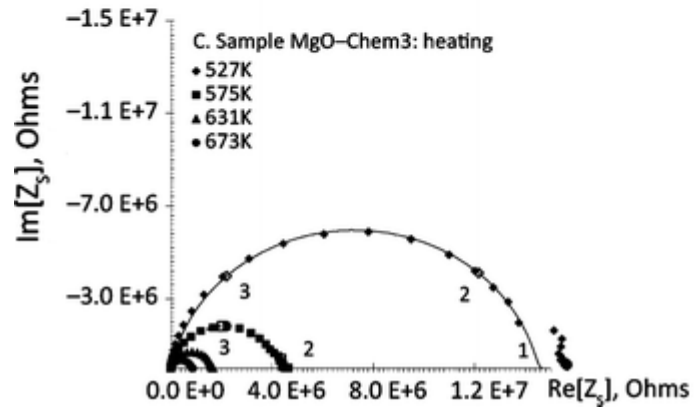
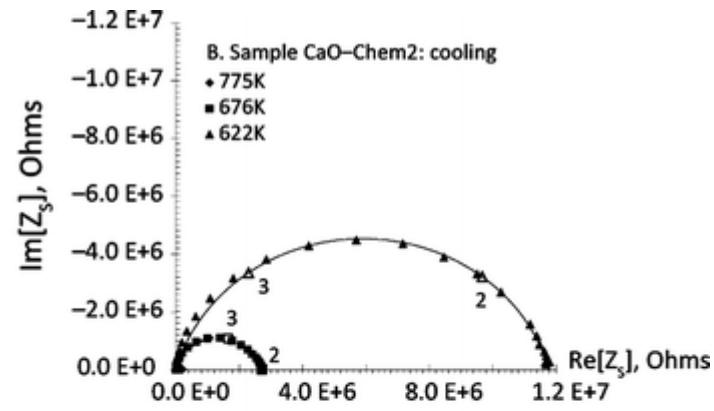
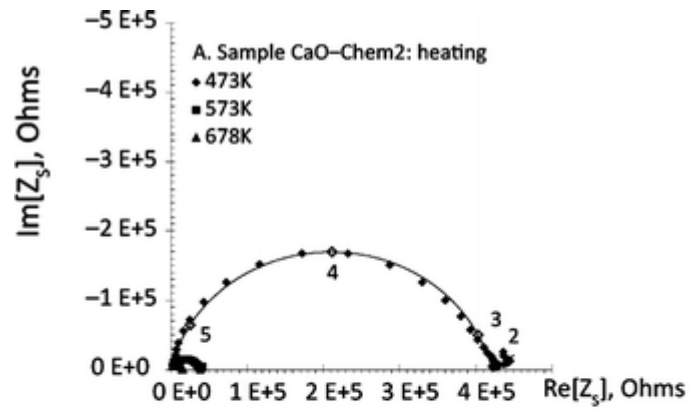


Figure 8

